Nickel binding with magnetite nanoparticles

Laura Fablet, Mathieu Pédrot, Fadi Choueikani, Isabelle Kieffer, Olivier Proux, Anne-Catherine Pierson-Wickmann, Vyria Cagnart, Takumi Yomogida, Remi Marsac

Nickel binding with magnetite nanoparticles

Laura Fablet[1,2], Mathieu Pédrot[1], Fadi Choueikani[2], Isabelle Kieffer[3], Olivier Proux[3], Anne-Catherine Pierson-Wickmann[1], Vyria Cagniart[1], Takumi Yomogida[4,5], Rémi Marsac[4]

[1] Univ Rennes, CNRS, Géosciences Rennes – UMR 6118, F-35000 Rennes, France

[2] Synchrotron SOLEIL, l'Orme des Merisiers, Départementale 128, 91190 Saint-Aubin, France

[3] Univ. Grenoble Alpes, CNRS, IRD, INRAE, Météo France, OSUG, 38000 Grenoble, France

[4] Université Paris Cité, Institut de physique du globe de Paris, CNRS, F-75005 Paris, France

[5]Nuclear Safety Research Center, Japan Atomic Energy Agency, 2-4 Shirakata, Naka, Tokai, Ibaraki, 319-1195, Japan

Environmental significance

Nickel is an omnipresent trace element in the environment. Due to its high affinity for iron oxide nanoparticles, its removal from soils and water using these nanoparticles represent a promising strategy, particularly with magnetites, which is naturally present in the environment. However, the interactions between Ni and magnetite remain poorly understood, because of the difficulty to control the stoichiometry (Fe(II)-to-Fe(III) ratio) of magnetite. The behavior of Ni in the presence of magnetite nanoparticles with varying stoichiometries, in aqueous solution and inert atmosphere, are probed by adsorption experiments and X-ray Absorption Spectroscopy. This study helps predicting the interactions between Ni and magnetite under environmental conditions, which can be used for the development of efficient remediation strategies.

Abstract

Nickel is generally found in trace amounts in the environment and can be beneficial to living organisms, but it is also an environmental contaminant of high concern, primarily due to anthropogenic releases. Fe oxides play an significant role in the behavior and fate of Ni in the environment, as they can interact with metal cations. However, the interactions between magnetite (Fe_3O_4) and Ni are not well described, and in particular the effect of magnetite stoichiometry (Fe(II)/Fe(III) = R) is not well considered. Ni adsorption experiments were performed on stoichiometric (R0.5) and oxidized (R0.1) magnetite as a function of Ni concentration and pH under anaerobic conditions. Samples were analyzed by transmission electron microscopy, X-ray absorption spectroscopy (XAS) and magnetic circular dichroism at the Ni $L_{2,3}$-edges and XAS at the Ni *K*-edge. At high Ni concentrations, Ni precipitates as $Ni(OH)_2$ on the magnetite surface, but also as distinct sheet-like particles. At low Ni concentrations, high energy resolution fluorescence detection (HERFD) XAS analyses at the Ni K-edge revealed Ni incorporation into R0.5 magnetite and surface adsorption of Ni onto R0.1 magnetite. The present results were compared with those previously published for Co, which revealed unexpected distinct behavior of Ni and Co. This element-specific binding mechanisms highlights the unique properties of magnetite compared to other naturally occurring iron oxides (e.g. goethite, hematite), for which Ni and Co binding mechanisms are similar. Taken together, these results will help predicting the behavior and fate of Ni under environmental conditions in the presence of magnetite, but also to synthesize magnetite nanoparticles doped by the addition of Ni with interesting magnetic properties.

Keywords. Nickel, surface speciation, magnetite, maghemite, X-ray absorption spectroscopy

Graphical abstract

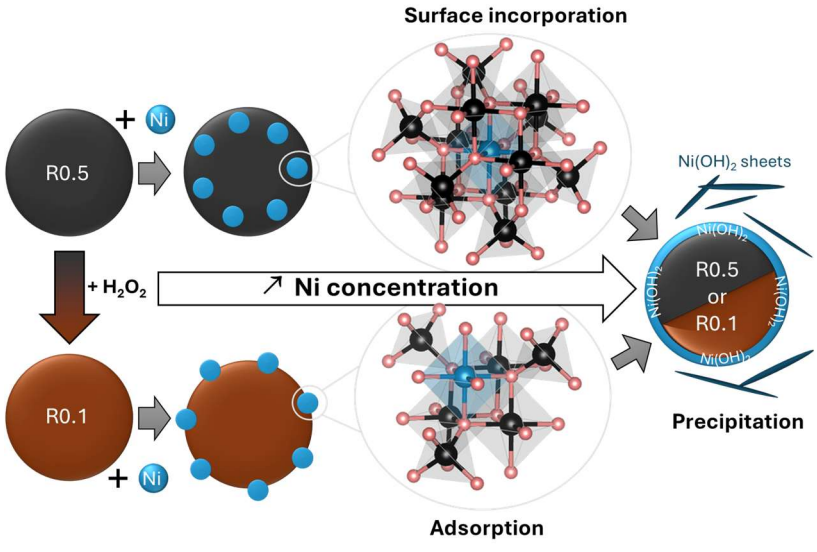

1. Introduction

Nickel is an ubiquitous trace element, widely distributed and essential for the functioning of numerous living organisms, playing a key role in vital processes such as enzyme activation in plants and microorganisms.[1–5] The natural concentration of Ni in soils and surface waters is generally less than 100 mg kg^{-1} and 0.005 mg L^{-1}, respectively.[3,6] However, its release into the environment is accelerated by anthropogenic activities such as fossil fuel combustion, mining, vehicle emissions and household and industrial waste disposal.[7,8] The Ni concentrations can reach up to 0.2 mg L^{-1} in polluted surface waters and 30 g kg^{-1} in polluted soils.[9,10] Its presence at high concentrations can be toxic to living organisms, whether in areas affected by anthropogenic discharges or naturally, in regions with a high pedogeochemical background level of trace elements.[3,11–13]

To remove metal contaminants, including Ni, from polluted water and soil, numerous strategies have been developed, such as adsorption-based procedures. The use of nanoscale structures, particularly magnetic Fe oxide nanoparticles like magnetite, has emerged as an effective tool for contaminants removal.[14–16] Indeed, magnetite nanoparticles can be manipulated with a magnetic field, enabling their recovery and reuse.[17,18] This ability, combined with their high surface-to-volume ratio and redox reactivity, makes them highly promising for applications in environmental remediation.[18,19] In addition, Fe oxides are naturally present in soils, sediments and waters in various forms (as magnetite, maghemite, hematite, etc.).[20] They are naturally formed through rock weathering,[20,21] but are also synthesized by certain living organisms, such as bacteria and plants.[22–24] These Fe oxides can significantly influence the fate of many contaminants,[25] sequestering them, thereby reducing their bioavailability and mobility.[20,26,27] Several studies have demonstrated that Ni surface speciation is specific to Fe oxide type,[28–32] which affects the Ni transport and fate in soils, sediments and waters.

However, the mechanisms controlling Ni interaction with magnetite in aqueous solutions relevant to natural systems have been poorly documented. Indeed, the majority of studies on the adsorption of Ni(II) on magnetite nanoparticles are carried out in O_2 atmosphere and/or with the use of oxidizing compounds, such as NO_3^- as background electrolyte,[33–38] which leads to the oxidation of Fe(II) to Fe(III).[39,40] In addition, a large number of studies were performed at pH < 7,[35–38] which favors the release of Fe(II) from the Fe_3O_4 structure.[41] The effect of magnetite

stoichiometry (R = Fe(II)/Fe(III)) does not only affect its redox reactivity but also the adsorption and surface speciation of ions (e.g. silicate, humic acid, quinolone antibiotics) on its surface.[42,43] In addition, stoichiometric magnetite (R0.5) surface is a better template for the formation of polynuclear Co species than non-stoichiometric (oxidized) magnetite (R0.1), whose adsorption seems to be limited by the absence of Fe(II) on the surface.[42,43] The lack of knowledge on Ni binding mechanisms onto magnetite hampers our capability to predict the environmental fate of Ni.

The present study examines Ni(II) sorption onto magnetite nanoparticles with distinct stoichiometries (R0.5 and R0.1). Isotherm experiments and modeling were conducted at pH 8 under inert atmosphere to preserve the initial magnetite stoichiometry and prevent Fe(II) oxidation or dissolution.[40,41] Additional adsorption experiments were performed across a pH range of 3-10. The surface speciation of Ni was probed by a comparison of soft X-ray absorption spectroscopy (XAS) and magnetic circular dichroism (XMCD) at the Ni $L_{2,3}$-edges,[40,41] as well as hard XAS with high energy resolution fluorescence detection (HERFD) at Ni *K*-edge (X-ray absorption near edge structure (XANES) and Extended X-Ray Absorption Fine Structure (EXAFS)) to assess Ni valence and local structure. Comparisons previously published results for Co(II),[42,43] which can be assumed as chemical analogue to Ni, provide insights into trace metals interactions with magnetite. This work enhances understanding of Ni speciation, and more broadly of metals, on magnetite nanoparticles with different stoichiometries, optimizing their application in water treatment, but also for the synthesis of Ni-doped nanoparticles for high-tech applications. Thus, a better prediction of nanomagnetite-Ni interactions provides better insight into Ni behavior in the environment, and their sorption capacity towards metals could enable their use to be optimized in several fields.

2. Materials and Methods

2.1. Chemicals

All chemicals used were purchased from Sigma-Aldrich and were of analytical grade or better. Sample solutions were prepared with Milli-Q ultrapure water (specific resistivity 18.2 MΩ cm). The pH of all the samples was adjusted by HCl and NaOH (no buffer was used). For TEM measurements, hexadecyltrimethylammonium bromide (CTAB) was used as a surfactant.

2.2. Synthesis of magnetite nanoparticles with various stoichiometry

All syntheses were performed in an anaerobic chamber (N_2-glovebox, Jacomex, $O_{2(g)}$<1 ppm) at room temperature, following a well-known co-precipitation method of iron salts.[40,44] All the solutions were purged with $N_{2(g)}$ for at least 12 h outside the glovebox before use. The full stoichiometric magnetite (R = 0.5) was synthesized with the dissolution of $FeCl_2$ and $FeCl_3$ in HCl solution, which was then added to NaOH solution leading to the instantaneous precipitation of ~10 nm magnetite nanoparticles. Non-stoichiometric nanoparticles (R = 0.1) were prepared by adding a known volume of H_2O_2 30% (V_{H2O2}) to R0.5 according to the following formula, which assumes the oxidation of two Fe(II) by one H_2O_2 molecule:

$$[H_2O_2] = \frac{[Fe(II)] - R \times [Fe(III)]}{2 \times (R+1)} \qquad (2)$$

With R = 0.1 is the target magnetite stoichiometry, [Fe(III)] and [Fe(II)] are the initial concentration in the stoichiometric magnetite suspension (mol L^{-1}). The synthesized solids were washed with ultrapure water (adjusted to pH ~8.5 with NaOH to avoid the release of Fe(II)). The stoichiometry of the synthesized nanoparticles was verified by spectrophotometric determination of dissolved [Fe(II)] and total [Fe] (i.e., [Fe(III)] + [Fe(II)]) by the 1,10-phenanthroline colorimetric method.[45]

2.3. Sorption experiments

Aqueous suspension of magnetite nanoparticles (R0.1 and R0.5) were prepared in 15 mL tubes with 10 mM NaCl for a total Fe concentration of 6.5 mM (~0.5 g L^{-1} magnetite). Isotherm experiments were performed at pH 8 and varying total Ni concentrations ($[Ni]_{tot}$) from 0.04 to 3

mM (using a 100 mM $NiCl_2$ stock solution) for R0.1 and R0.5. After 7 days of equilibrium, a magnet was used to collect the solid fraction of all the samples. The supernatant was filtered through 0.2 µm PES filters (Sartorius Minisart) that were pre-rinsed with a portion of the same supernatant. Ni concentrations in the aqueous solution after filtration ($[Ni]_{aq}$) were determined by ICP-MS (Agilent Technologies 7700X). Before Ni quantification, calibration curves were recorded and validated using certified materials references (SLRS-6, National Research Council). A rhodium solution was used as an internal standard to correct the instrumental drift and potential matrix effects. The limit of Ni quantification was determined at 15.2 ng L^{-1} (AFNOR Certification).[46] The total amount of Ni associated with the solid phase was expressed in terms of Ni surface density onto $Fe_{3-\delta}O_4$ ($[Ni]_s$ in atoms per nm^2) and calculated as follows:

$$[Ni]_s = ([Ni]_{tot} - [Ni]_{aq}) \times \frac{V}{m} \times \frac{1}{SSA} \times N_A \times 10^{-1} \qquad (3)$$

where $[Ni]_{tot}$ and $[Ni]_{aq}$ are given in mol L^{-1}, V is the sample volume (L), m is the magnetite mass (g), SSA is the surface specific area (m^2 g^{-1}) and N_A is the Avogadro constant (mol^{-1}). On the basis of repetition of some experiments, uncertainty associated with Ni adsorption was 5 %. A nickel ferrite suspension was prepared by following the magnetite synthesis method (see section II.2), replacing 10 % of the Fe(II) ($FeCl_2.4H_2O$) with Ni(II) ($NiCl_2.6H_2O$), in a N_2-glovebox at room temperature. NaOH (0.1 mol L^{-1}) was added until the pH was stable at 8.5 and the solution was kept as is. A Ni hydroxide suspension was prepared from the 100 mM $NiCl_2$ stock solution, which was neutralized by adding NaOH 1M until precipitation. NaOH was added until the pH was stable at 10 and the solution was kept as is.

2.4. Characterization by TEM

Magnetite nanoparticles (R0.1 and R0.5) were characterized by transmission electron microscopy (TEM; JEOL JEM 2100 HR microscope; accelerating voltage = 200 kV), for four Ni concentrations ($[Ni]_{tot}$ = 0.04, 0.2, 0.8 and 3 mM). A small volume of Ni-magnetite was collected and a surfactant (CTAB, 1 mM) was added in each sample to limit particle aggregation, which was then diluted with ultrapure water, at pH 8. Each sample was sonicated for 15 min. A droplet of the diluted suspension was deposited on a Holey carbon film 300 mesh copper grid and dried inside an anaerobic chamber. Samples were transported to the microscope in hermetically sealed glass bottles, preserving them under a N_2 atmosphere. The average particle diameter of the pristine

magnetite was found to be 11.5 ± 1.5 nm for R0.5 and 9.6 ± 2.6 nm for R0.1 by measuring 100 particles.[40,41]

2.5. Soft XAS and XMCD analyses

The dried samples were analyzed by soft XAS and XMCD, probing the $L_{2,3}$-edges (2p → 3d) of Fe and Ni. XAS and XMCD analyses are chemically selective and sensitive to valence states and help to better understand the contribution of Ni and Fe cations to the structure and magnetic behavior of nanoparticles. XAS and XMCD spectra were recorded on the DEIMOS beamline at synchrotron SOLEIL.[47] Measurements were carried out on dried nanoparticles by drop-casting of colloidal suspensions on silicon plates at room temperature in an Ar-glovebox (Jacomex $O_{2(g)} < 1$ ppm) connected to the DEIMOS endstation. The silicon plates were fixed to a copper sample holder, which was then introduced into the superconducting magnet. All the spectra were collected in total electron yield (TEY) at 4.2 K and under UHV conditions (10^{-10} mbar). XAS spectra were recorded by reversing the full circular polarization of the X-rays to the right (σ_R) or left (σ_L), and by varying the external magnetic field (H = +6 or −6 T). Isotropic XAS spectra were plotted as ($\sigma^+ + \sigma^-$)/2, while the XMCD results were plotted as ($\sigma^+ - \sigma^-$), where $\sigma^+ = [\sigma_L(H^-) + \sigma_R(H^+)]/2$ and $\sigma^- = [\sigma_L(H^+) + \sigma_R(H^-)]/2$. For all the Ni spectra, the background of XAS and XMCD at the Ni $L_{2,3}$-edges were corrected with the software OriginPro. XAS and XMCD were normalized by dividing the raw signal by the edge jump of the isotropic XAS. By measuring XMCD intensity as a function of the external magnetic field (from +6 to -6 T), XMCD magnetization curves at specific sites on the Ni L_3-edge were plotted. At DEIMOS beamline, fully circularly polarized X-rays were provided by an Apple-II HU52 undulator for XAS and XMCD, while EMPHU65 with a polarization flipping rate of 10 Hz was used to record the magnetization curves. The beam size was 800 × 800 μm^2 and the photon energy resolution was 100 meV.

The XMCD at the Fe L_3-edge presents three peaks which can be used to estimate the amount of Fe(II) and Fe(III) and then the magnetite stoichiometry of the samples. The evolution of peak intensities were monitored using the S indicator: [40,48]

$$S = \frac{(S_1+S_2)}{(S_2+S_3)} \qquad (4)$$

where S_1 peak is due to the contribution of Fe(II) and Fe(III) in Oh coordination, with a dominance of Fe(II). The S_2 peak corresponds to Fe(III) in Td sites and the S_3 peak corresponds to Fe(III) in Oh sites. The S indicator was then used to calculate the effective stoichiometry according to the method described by Jungcharoen *et al*. (2021).[40]

2.6. *K*-edge XAS experiment

Hard XAS experiments were performed in High Energy Resolution Fluorescence Detection (HERFD) mode on FAME-UHD beamline (BM16) at the ESRF. Beamline is built with a 2-crystal Si220 monochromator surrounded by two Rh-covered Si mirrors. The first crystal of the monochromator is liquid-nitrogen cooled. The second crystal is dynamically bent, in the sagittal plane, to horizontally focus the beam on the sample. The two mirrors aim at filtering the high energy photons, and so allow to remove the harmonics from the monochromatic beam. Moreover, the first mirror collimates the beam in the vertical direction while the second mirror focusses the beam on the sample. Thanks to these optical elements the monochromatic beam on the sample has an optimum energy resolution, close to the intrinsic resolution, and the beam-size is around 200 x 100 μm² (Full Width Half Maximum values) still on the sample.

Fluorescence detection was performed using a crystal-analyzer spectrometer in Johann-Johansson geometry, equipped for this experiment with five Si620 crystals (radius of curvature: 1m). The crystals were optimized to select the Ni $K_{\alpha 1}$ emission line (7.478 keV), i.e. with a Bragg angle around 74.88°. Photons reflected by the crystals were focused on an energy-resolved detector (Silicon Drift Detector) allowing to discriminate the diffracted photons of interest (Ni $K_{\alpha 1}$) from the scattered ones (here mainly the Fe K_α and Fe K_β lines) and so to optimize the signal-to-background ratio. Energy calibration of the incident beam was ensured by measuring the XAS spectrum of a metallic Ni foil. The 1st maximum of the spectrum 1st derivative was set to 8.333 keV. Energy bandwidth of the entire setup (including both the beamline and the spectrometer contributions) was estimated to 0.8 eV by measuring the elastic peak. The magnetite-Ni samples were mixed with boron nitride to prepare pastilles of 5 mm in diameter, in a glove box. During data acquisition, the samples were put in a glove bag with a continuous flow of N_2 in order to limit their oxidation. Moreover, the position of the beam on the sample was changed between each acquisition to preserve the sample from radiation damages.

2.7. XANES simulation

To estimate the change of the XANES spectra at the Ni *K*-edge of Ni bound to magnetite or precipitated as $Ni(OH)_2$, theoretical modeling of Ni *K*-edge XANES spectra was conducted by the finite difference method for near-edge structure (FDMNES).[49] The code allows the calculation of the occupied and unoccupied projected density of states in relation to the X-ray absorption and emission processes. $Ni(OH)_2$ and the $NiFe_2O_4$ were selected as model compounds. Simulations were performed using an atomic cluster with 6.0 Å for $Ni(OH)_2$ and the $NiFe_2O_4$, respectively. Calculations were performed with dipole transitions and no experimental broadening was included.

2.8. Chemical speciation modeling

Aqueous chemical speciation calculations were performed using the geochemical code PHREEQC (version 2)[50] and the Minteq.v4 database, which accounts for the relevant complexation reaction for Ni^{2+} with Cl^- on OH^-. Ionic strength effects on equilibrium constants were calculated using the Davies equation.

3. Results and Discussion

3.1. Investigations of Ni sorption to magnetite

Ni sorption to R0.1 and R0.5 at pH 8 was studied as a function of Ni concentration (Fig. 1a). A log scale is used in Fig. 1b to visualize the Ni sorption behavior at trace levels. The correspondence between the total ($[Ni]_{tot}$), solid ($[Ni]_s$) and aqueous ($[Ni]_{aq}$) Ni concentrations is presented in Table S1. For both stoichiometries, Ni sorption isotherm reveals two steps. First, a strong sorption behavior until a plateau is reached at relatively low concentration ($[Ni]_{aq} < 0.1$ mM), which can be attributed to several processes including incorporation, monomers or polymers formation at the magnetite surface.[51–55] For R0.5, the sorption is relatively strong at trace levels (Fig. 1b) and the plateau is reached at ~4 atom nm^{-2} (Fig. 1a,b), whereas Ni sorption is much weaker and the plateau is reached for a smaller surface loading for R0.1 (~1 atom nm^{-2}). This points to a strong effect of magnetite stoichiometry on Ni adsorption, as previously shown for other ions.[42,43,56] Previous studies dedicated to Ni adsorption on non-stoichiometric magnetite nanoparticles determined a maximal sorption capacity of 1.18 atom nm^{-2} at pH 8, which is a value close to that of R0.1.[34] The second sorption step is characterized by an increased sorption at high Ni concentration, suggesting $Ni(OH)_2$-like phase precipitation, as commonly observed for Ni or other metal ions onto Fe-oxides.[51,57–60] Results obtained for R0.1 and R0.5 at high [Ni] are very similar suggesting the formation of similar Ni-containing compounds.

The Ni sorption isotherms are compared to the Co sorption data of Fablet *et al*. (2024), collected for R0.1 and R0.5, following the same experimental protocol (Fig. 1a,b).[43] At trace levels (Fig. 1b), Ni sorption to R0.5 is similar Co sorption to R0.1 and R0.5, hence suggesting similar sorption processes, i.e., surface complexation of Ni/Co as monomers or their incorporation into magnetite nanoparticles, a previously concluded for Co.[42,43] The much weaker interaction of Ni than Co with R0.1 is contrary to what can be expected by considering surface complexation process only. Indeed, metal cation surface complexation to ≡Fe-OH groups generally follows the hydrolysis behavior of the cation [51,61]; and Ni^{2+} hydrolysis constant (K = 9.86)[62] is larger to that of Co^{2+} (K = 9.61).[63] Therefore, our results suggest that Ni incorporation into oxidized magnetite is less favorable than Co, which might arise from the more similar ionic radius of Co^{2+} and Fe^{2+},[64] as well as the redox behavior of both Co(II,III) and Fe(II,III), by contrast with Ni(II). In the case of R0.1,

Ni sorption might mainly be driven by surface complexation rather than incorporation. These observations are confirmed on a larger pH range in Fig. 1c, which compares the adsorption of Ni with Co for the same concentration ([Co] or $[Ni]_{tot}$ = 0.04 mM).

The sorption plateau at intermediate Co concentrations was attributed to surface Co-polymer formation.[42,43] As the sorption of Ni weaker than that of Co both on R0.1 and R0.5 (Fig. 1a,b), it can be concluded that Ni-polymerization on magnetite nanoparticles is less favorable than that of Co. The sorption plateau at smaller values for R0.1 than R0.5 might suggest that surface vacancy sites, that may occur on maghemite, are not in favor of surface polymerization of divalent transition metals. These observations are confirmed on a larger pH range in Fig. 1d, for $[Co]_{tot}$ or $[Ni]_{tot}$ = 0.4 mM, which shows that Co-polymer formation onto R0.1 or R0.5 remains larger than that of Ni. This is further confirmed at the largest [Ni] or [Co] investigated, where Ni precipitation process occurs at larger [Ni] than [Co] with R0.5 although Ni solubility is expected to be smaller than that of Co in water according to solubility calculations with PHREEQC. Hence, it can be concluded that magnetite surface serves as a better template for Co than for Ni precipitation. Indeed, unlike Co, which has been shown to precipitate as an homogeneous layer around the magnetite nanoparticles, it has been shown, during synthesis of core@shell particles by thermal decomposition, that NiO develops only on specific crystallographic faces of the magnetite, forming an octopod shell with extended corners.[65] In addition, while Co surface precipitation was larger on R0.5 than on R0.1, the similar behavior of Ni with R0.5 and R0.1 could point out to significant $Ni(OH)_2$-like phase precipitation in homogeneous solution. This was confirmed by TEM analysis, as shown in Fig. S1, with the corresponding energy-dispersive spectroscopy (EDS) spectra for two extreme Ni concentrations ($[Ni]_{tot}$ = 0.04 and 3 mM) for R0.1 and R0.5. At low Ni concentrations ($[Ni]_{tot}$ = 0.04 mM), magnetite nanoparticles display the same characteristics as those observed in a previous study on Co,49 with no impact from the presence of Ni, for both stoichiometries. In contrast, for the highest concentration ($[Ni]_{tot}$ = 3 mM), numerous crystallized Ni sheets can be observed for both stoichiometries. Natile and Glisenti (2003) had also observed that NiO precipitates developed as isolated particles rather than precipitating on Co_3O_4 particle,[66] while Tougerti *et al.* (2012) showed that Al oxide is a good template for precipitation of other Ni phase.[67] Taken together, these results show that surface precipitation mechanism is ion- and phase-dependent.

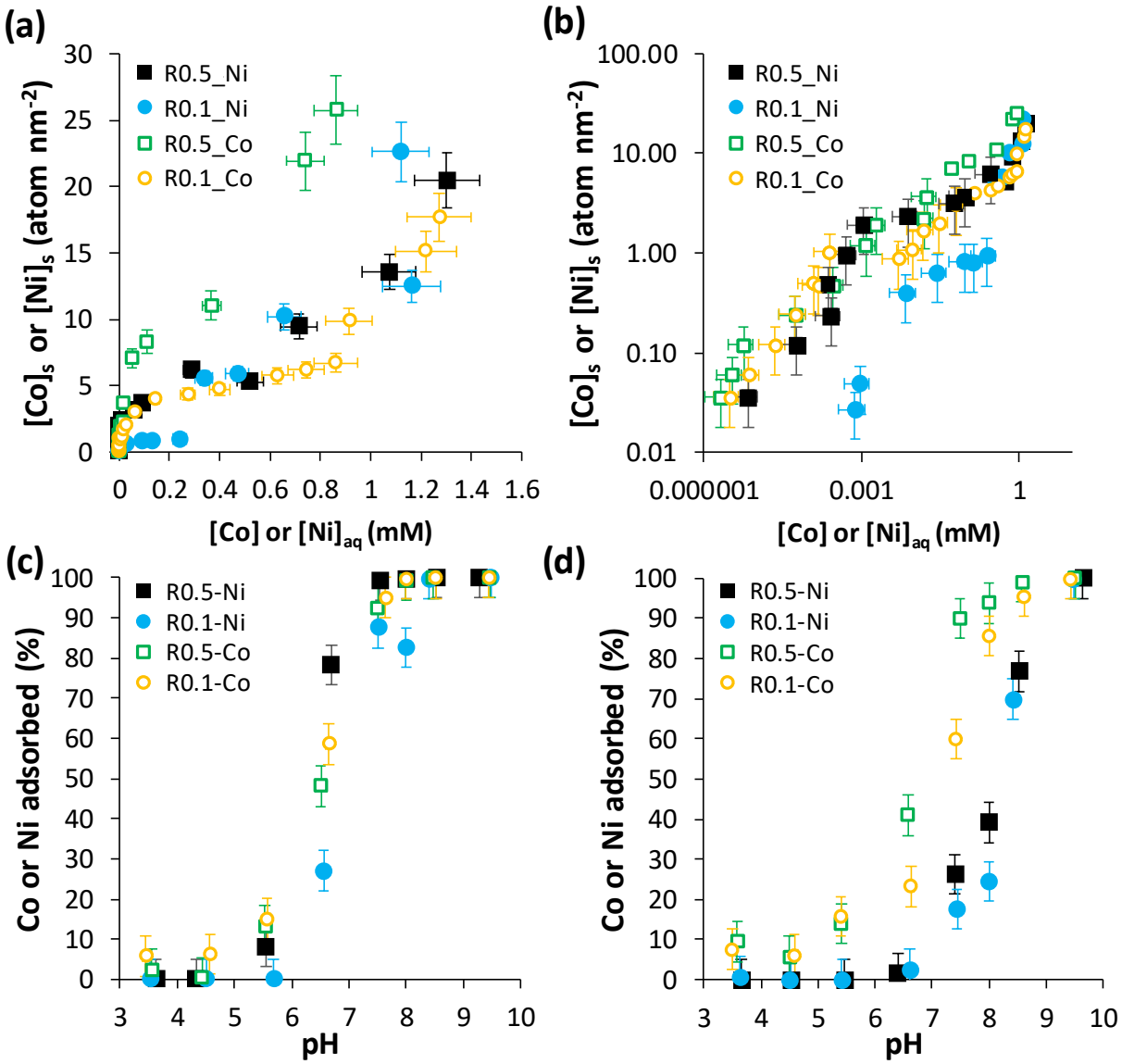

283

284 **Fig. 1** Comparison of Co ([Co]) and Ni ([Ni]) adsorption on R0.1 and R0.5, at pH 8 in 10 mM NaCl using (a) linear and (b)
285 logarithmic scale. Effect of pH on the percentage of Co or Ni adsorbed on R0.1 and R0.5, for (c) $[Co]_{tot}$ or $[Ni]_{tot}$ = 0.04 mM and
286 (d) $[Co]_{tot}$ or $[Ni]_{tot}$ = 0.4 mM. The black squares correspond to Ni on R0.5, the blue circles to Ni on R0.1, the green empty squares
287 to Co on R0.5 and the yellow empty circles to Co on R0.1. Data for Co are from Fablet *et al.* (2024).[43]

288
289

The experimental Ni sorption data are compared with model results obtained by the combination of a Langmuir and a Freundlich adsorption isotherm equations, with the following equations:[41]

$$[Ni]_s = Q_L + Q_F \qquad (5)$$

where Q_L and Q_F are magnetite-bound Ni amounts. Eqn (4) describes Q_L:

$$Q_L = Q_{max} \frac{K_L[Ni]_{aq}}{1+K_L[Ni]_{aq}} \quad (6)$$

where Q_{max} is the adsorption capacity (here in atom per nm^{-2}) and K_L is the Langmuir constant (in L $mmol^{-1}$). Eqn (5) describes Q_F:

$$Q_F = K_F[Ni]_{aq}^n \qquad (7)$$

where K_F is the Freundlich constant, and n is the non-ideality parameter. Results of the fit are shown in Fig. 2. The parameters of eqn (3)-(5) for both stoichiometry are shown in Table 1. For Ni onto R0.5, surface complexation, incorporation and polymer formation are together modeled with a single Langmuir equation (by contrast with Co that required two Langmuir ones)[66] characterized by Q_{max} is equal to 2.30 atom nm^{-2} with log K_L = 3.14. For R0.1, model results define Q_{max} = 0.96 atom nm^{-2} and log K_L = 1.76. The Q_{max} value of Ni for R0.1 is close to that of the first Langmuir equation of Co (Q_{L1} = 0.52 atom nm^{-2} for R0.1 and R0.5), which further points to the fact that Ni-polymer formation is very limited at R0.1 surface. Parameters for the Freundlich equation are similar between both stoichiometries with Ni, as expected from the similar sorption data. Overall, the model combining the two adsorption isotherm models well predicted the experimental results. However, as already pointed out,[40,41] the present model is here used as a semi-quantitative guide to interpret isotherm and spectroscopic data taking into account several distinct surface species. It cannot be considered as a predictive model of the interaction of metals with magnetite because it does not include several key parameters, such as electrostatic contribution for example.

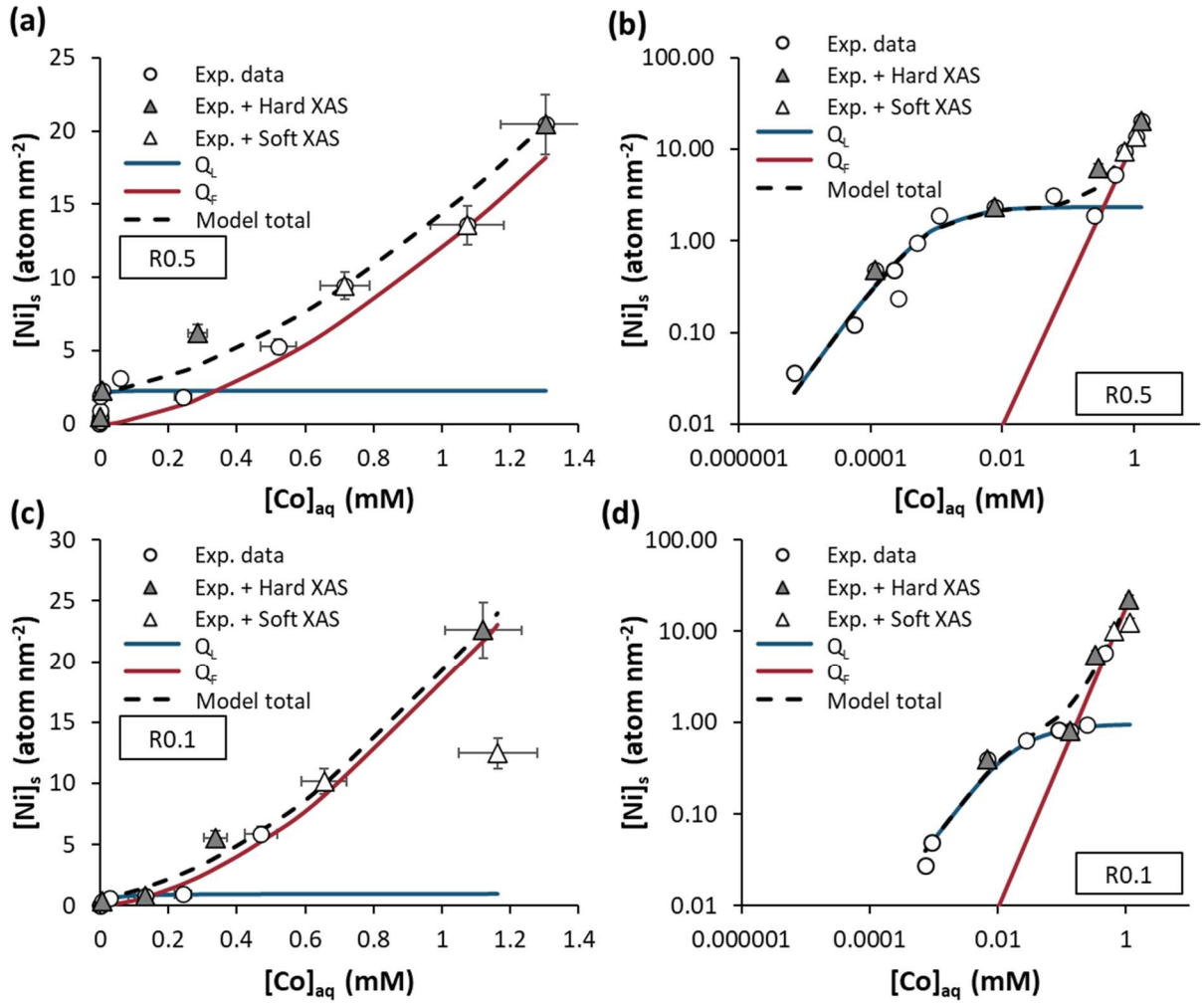

Fig. 2 Ni adsorption isotherm on R0.5 (a,b) and R0.1 (c,d) (0.5 g L^{-1}) presented as linear (a, c) and logarithmic scale (b, d), at pH 8 in 10 mM NaCl, The points represent the experimental data ("Exp. data"), represented by circles and triangles. The data represented by a triangle were analyzed by hard XAS and data with a gray triangle are also analyzed by soft XAS. Dashed lines are the model results using a combination of a Langmuir (blue line), and a Freundlich (red line) isotherm equations.

Table 1 Optimized parameters of equation X, for Langmuir model (L) and Freundlich model (F), for R0.1 and R0.5. Q_{max} is the adsorption capacity (atom nm^{-2}).

Stoichiometry	Parameters	Langmuir (L)	Freundlich (F)
R0.1	**n**	-	1.64
	log K	1.76	0.17
	Q_{max}	0.96	-
R0.5	**n**	-	1.55
	log K	3.14	0
	Q_{max}	2.30	-

3.2. Nickel speciation by XAS and XMCD at $L_{2,3}$-edges

The speciation of Ni bound to R0.5 and R0.1 was studied at several Ni concentrations by XAS (Fig. 3a and b respectively) at Ni $L_{2,3}$-edges. Raw XAS spectra are also shown in Fig. S2. The XAS spectra show two contributions at L_3-edge at around 850 eV (peak A) and 852 eV (peak B), and a double peak at L_2-edge at 866.8 eV (peak C) and 868.2 (peak D). The presence of these multiple peaks are characteristic of the doublet structure of Ni(II).[68–70] All XAS spectra were normalized to the intensity of peak A in order to study the evolution of the other peaks. For both stoichiometries, as the Ni concentration increases, the XAS spectra show an evolution of the intensity of peaks B and D, as well as a decrease in peak C. Thus, spectra at low [Ni] tend to resemble the spectrum of the $NiFe_2O_4$ reference while spectra at high [Ni] are similar to that of the $Ni(OH)_2$ reference. It should be noted that at low Ni concentrations ($[Ni]_s$ = 0.5 atom nm^{-2} for R0.5 and 0.4 atom nm^{-2} for R0.1), the intensity of peak B is larger for R0.1 than R0.5. Furthermore, the spectra of R0.5 and $NiFe_2O_4$ are quite similar, except a slightly less intense peak B for R0.5, whereas the spectrum of R0.1 shows more intense B and D peaks than that of $NiFe_2O_4$. These results suggest that at low concentrations, Ni does not form the same species on R0.1 as on R0.5, which is in line with the interpretation of isotherm data, pointing to a favored Ni incorporation (i.e. $NiFe_2O_4$-like phase formation) into R0.5. On the other hand, at high Ni concentration ($[Ni]_s$ = 20.4 atom nm^{-2} for R0.5 and 22.6 atom nm^{-2} for R0.1), both stoichiometries present a spectrum almost identical to that of $Ni(OH)_2$, indicating the formation of a precipitate, as distinct particles and/or at magnetite surface,

which is consistent with the adsorption isotherm data. The presence of a ferrimagnetic phase ($NiFe_2O_4$-like) at low [Ni], followed by the formation of an antiferromagnetic ($Ni(OH)_2$-like) phase at high [Ni] is an interpretation also supported by XMCD investigations, as detailed in SI (Fig. S3 and S4), because (i) XMCD signal intensity decreases with increasing [Ni] and (ii) Ni-specific magnetization curves show saturation and absence of saturation at low and high [Ni], respectively, which is characteristic of ferrimagnetic (e.g. $NiFe_2O_4$) and antiferromagnetic phase (e.g. $Ni(OH)_2$). The XAS and XMCD spectra at the Fe $L_{2,3}$-edges are presented in Fig. S5, and are consistent with previous reports for R0.1 and R0.5.[40,41] No significant effects of Ni is observed on Fe speciation, probably because the small amount of Ni with respect to Fe in the solid phase, as observed for Co.[42,43]

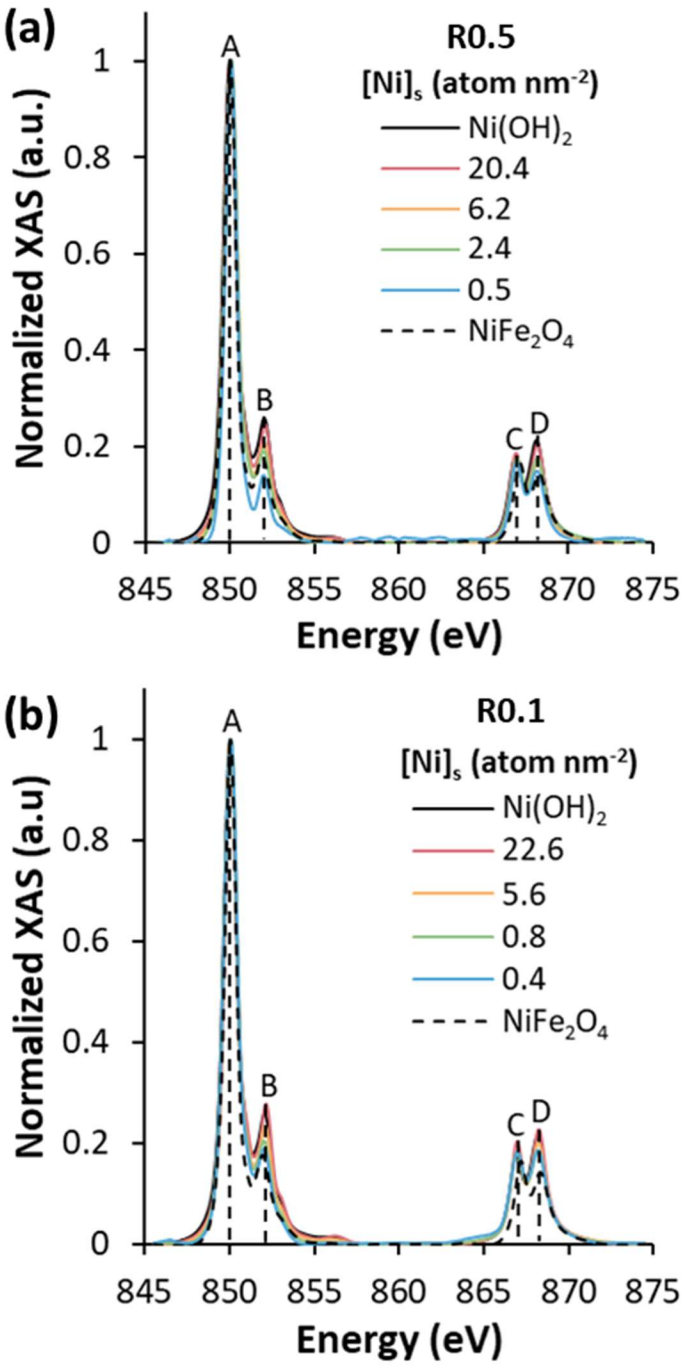

Fig. 3 Normalized XAS spectra at the Ni $L_{2,3}$-edges, at 4.2 K and under 6.4 T for (a) R0.5 and (b) R0.1 with different Ni content ($0.4 \leq [Ni]_s \leq 22.6$ atom nm^{-2}) and two references: $NiFe_2O_4$ (dotted line) and $Ni(OH)_2$ (full black line). XAS signals are normalized to the maximum peak.

3.3. Structure of Ni surface species probed by HERFD-XAS at *K*-edge

In order to further understand the difference on the adsorption mechanisms of Ni onto R0.1 and R0.5, the Ni speciation was probed by HERFD-XAS at Ni *K*-edge. The XANES spectra of the

samples with different solid concentrations ($[Ni]_s$ = 0.4 to 22.6 atom nm^{-2}) are presented in Fig. 4a,b. XANES spectra exhibit a main peak at 8351.6 eV, accompanied by a shoulder at 8349 eV, corresponding to the transition 1s → 4p. For both R0.1 and R0.5, the shoulder increases in intensity as the solid Ni concentration increases. For the highest $[Ni]_s$, the spectra are similar to that of the $Ni(OH)_2$ reference. However, at any [Ni] the shoulder is greater for R0.1 than for R0.5. The Ni *K*-edge spectra exhibit a small pre-edge absorption peak, corresponding to the transition 1s → 3d (Fig. 4c,d). The pre-edge is composed of a main peak, at 8333.3 eV, which corresponds to the Ni present on Oh sites,[71] and a second peak at 8337 eV for low Ni concentrations. The second peak decreases and disappears as Ni concentration increases. In the case of R0.5, the pre-edge spectrum of $[Ni]_s$ = 0.5 atom nm^{-2} is very close to that of $NiFe_2O_4$.[72] Figure S6 shows the theoretical XANES Ni *K*-edge spectra of $Ni(OH)_2$ and $NiFe_2O_4$. In the XANES simulation, the intensity of the 1st peak around 8346 eV is strong for $Ni(OH)_2$, which is consistent with the features of the XANES experimental spectra of R = 0.5 with high Ni concentration (Fig. 4a). When Ni is in the magnetite structure ($NiFe_2O_4$-like structure), the intensity of the 1st peak of the simulated XANES spectrum decrease and the intensity of the 2nd peak around 8350 eV increase, which is consistent of the feature of XANES spectra of R0.5 with low Ni concentration (Fig. 4a). These results support that the occurrence of Ni in magnetite-like structure for low Ni concentration with R0.5. For the same Ni solid concentration ($[Ni]_s$ = 0.4 atom nm^{-2}), R0.1 shows a similar pre-edge feature at 8333.3 eV, but the one at 8337 eV is less intense than that of R0.5. At high Ni concentrations, the spectra for R0.1 and R0.5 are similar and close to that of the $Ni(OH)_2$ reference, in accordance with the formation of a precipitate. These results are in line with the Ni $L_{2,3}$-edges XAS and XMCD data presented above.

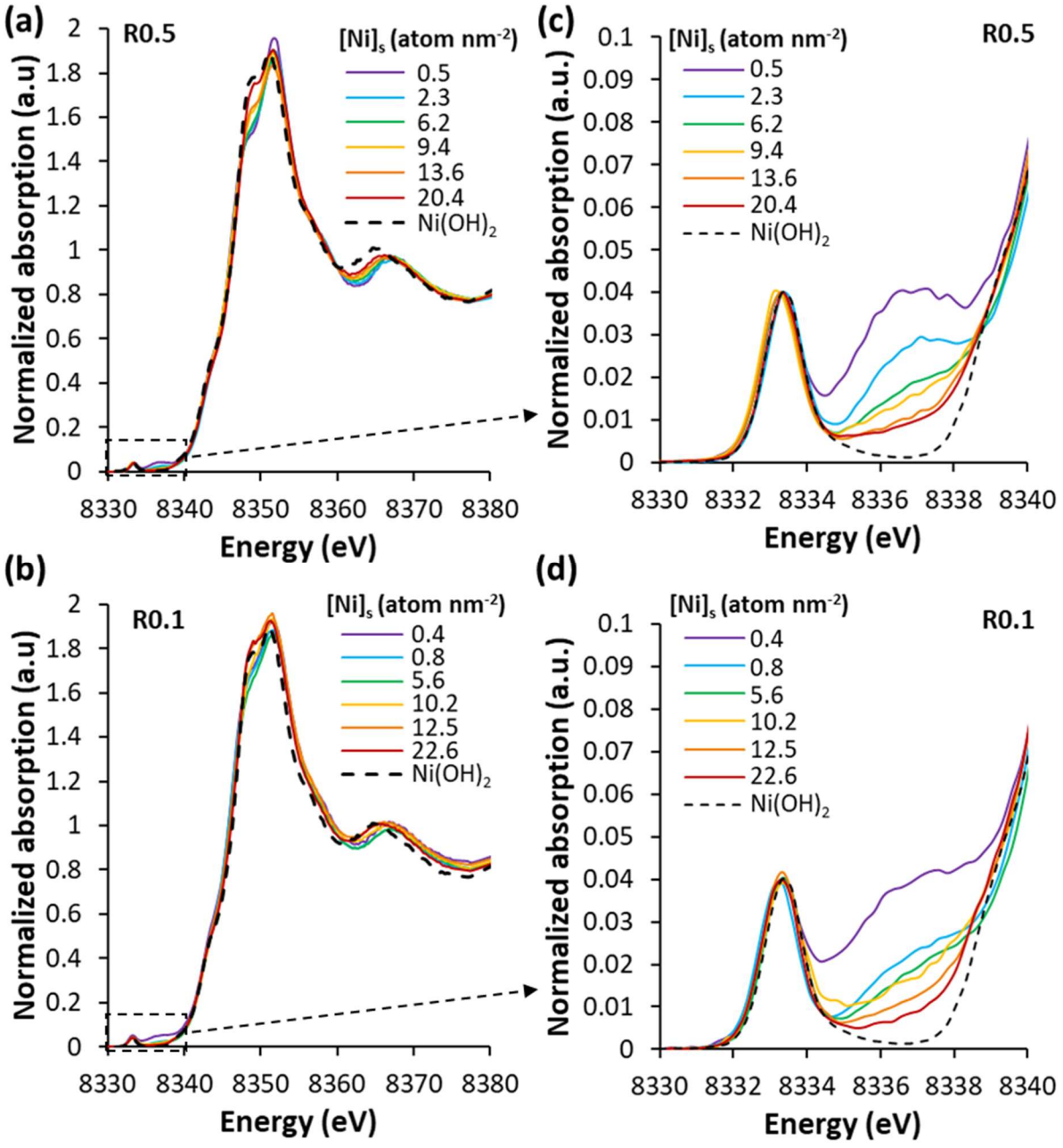

383

384 **Fig. 4** XANES spectra obtained for different Ni solid concentration (from 0.4 to 22.6 atom nm^{-2}) for (a) R0.5 and (b) R0.1, and
385 a zoom on the pre-edge feature between 8330 and 8340 eV for (c) R0.5 and (d) R0.1. The reference of $Ni(OH)_2$ is illustrated in
386 dotted lines.

387

388 The k^3-weighed EXAFS spectra for the samples with different Ni concentrations ($[Ni]_s$ = 0.4 to
389 22.6 atom nm^{-2}) for R0.5 and R0.1 are shown in Fig. 6a,b. The EXAFS spectra of R0.5 (Fig. 5a)
390 and R0.1 (Fig. 5b) present characteristic features, which evolve as the concentration of solid Ni
391 increases and shifts slightly. At high concentrations, for both R0.1 and R0.5, the spectra are similar
392 to those of $Ni(OH)_2$. The characteristic features in the EXAFS spectra at low [Ni] are less
393 pronounced for R0.1 than for R0.5. For R0.5 and low Ni concentration, the spectrum is similar to
394 that found for Ni substituted on Oh sites in the magnetite.[73] The corresponding Fourier-transform
395 (FT) of EXAFS spectra are shown in Fig. 5c for R0.5 and Fig. 5d for R0.1. The distance of the
396 first shell of the FT at ~1.5 Å corresponds to a Ni-O interaction and the second at ~2.7 Å to a Ni-
397 Fe or Ni-Ni interaction.[74,75] Indeed, as Fe and Ni have very close atomic number (ΔZ=2), similar
398 ionic radii and form similar local structures, it is difficult to differentiate them.[31] At low and
399 medium Ni concentrations, a third shell is distinguished at ~ 4.66 Å. The FT at low concentrations
400 for R0.5 are similar to the spectra found for Ni ferrites, with the presence of three shells.[73] As the
401 Ni concentration increases, the spectra are more and more similar to that of the measured $Ni(OH)_2$
402 reference. The same behavior is observed on R0.1, but third shell is hardly detected.

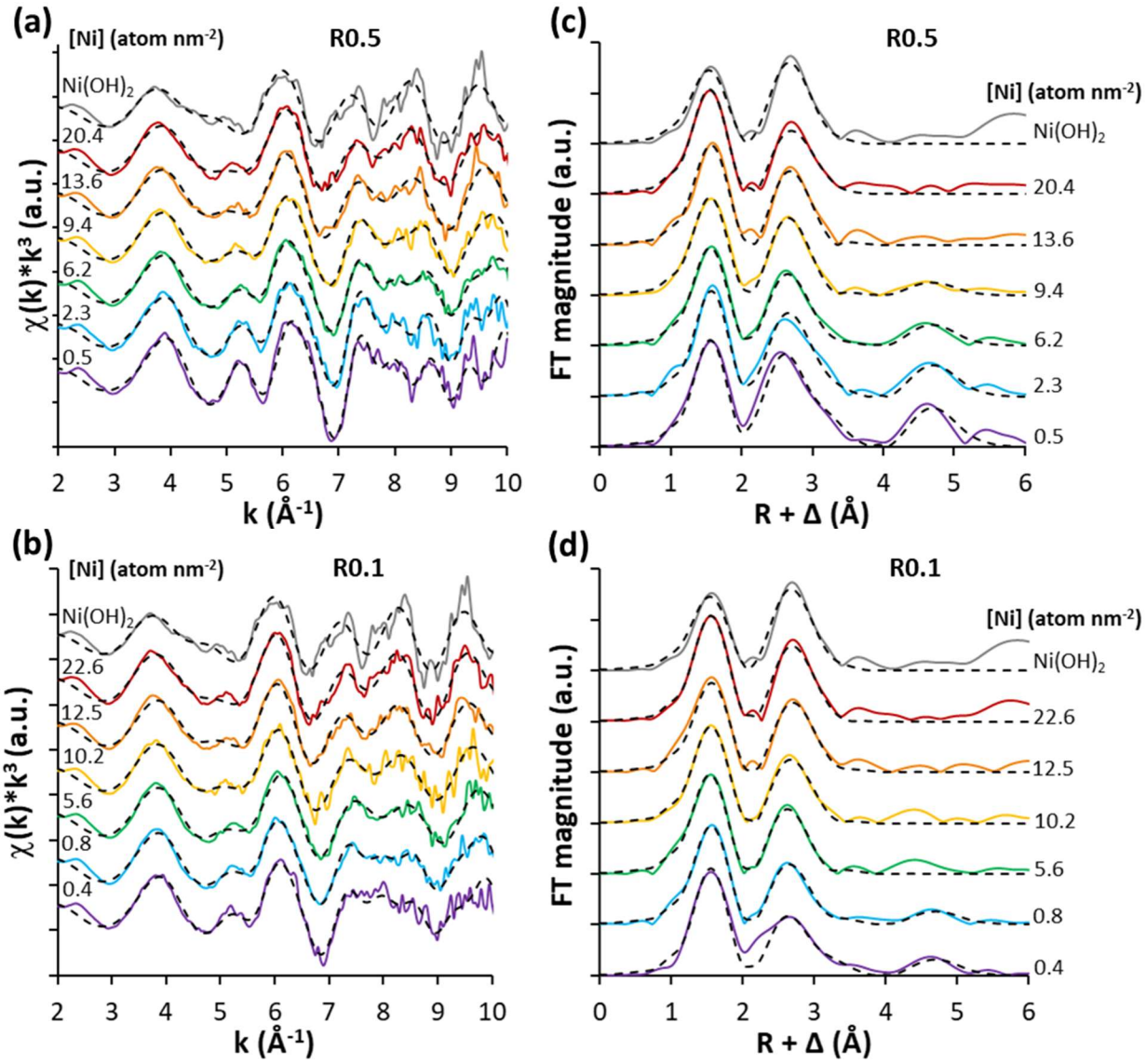

Fig. 5 EXAFS spectra obtained for different Ni solid concentration (from 0.4 to 22.6 atom nm^{-2}) and $Ni(OH)_2$ reference for (a) R0.5 and (b) R0.1, and the corresponding Fourier Transform for (c) R0.5 and (d) R0.1, plotted with the fit results reported as dotted lines.

EXAFS spectra were fitted to accurately probe the speciation of Ni in presence of R0.5 and R0.1, as well as $Ni(OH)_2$ reference. The fits are plotted in Fig. 5, and the parameters for the two extreme concentrations are presented in Table 2 for $Ni(OH)_2$ and for both stoichiometries. The parameters for the other concentrations are presented in Table S2 and Table S3 for R0.5 and R0.1, respectively. The EXAFS of $Ni(OH)_2$ spectrum was fitted with ~6 O at 2.04 Å and a 6 Ni at 3.09 Å, in agreement with literature data for $Ni(OH)_2$ particles, in which Ni is octahedrally coordinated to O, and shares edges with other Ni octahedrons.[76,77] For all samples, ~6 O are found at 2.05 ± 0.01 Å. For R0.5, at low Ni concentration ($[Ni]_s$ = 0.5 atom nm^{-2}), three different Ni-Fe/Ni paths were determined. An initial fit indicated a coordination number of ~6 for all three paths, which were then constrained to the same value. The first two Ni-Fe/Ni paths were found at 2.98 and 3.52 Å, contributing to the second coordination sphere (Table 2). These distances correspond to those found for Ni-Fe_{Oh} (between 2.92 and 2.94 Å) and Ni-Fe_{Td} (between 3.44 and 3.51 Å) bonds in nickel ferrites.[78–81] A third Ni-Fe/Ni path is found at 5.14 Å in agreement with literature data for nickel ferrites.[78] These results suggest that, at low Ni concentrations, Ni is incorporated into stoichiometric magnetite nanoparticles. As the [Ni] increases, the number of neighbors in the second shell decreases from 6.2 to 3.8, while the interatomic distance of the first Ni-Fe/Ni path increases from 2.98 to 3.07 Å. The distance of the second Ni-Fe/Ni path remains constant (3.57 ± 0.05 Å). In addition, the number of neighbors for the third Ni-Fe/Ni path decreases up to $[Ni]_s$ = 9.4 atom nm^{-2} before disappearing. These changes in coordination number indicate that Ni in Oh symmetry is increasing with respect to Td one, in line with the transition from $NiFe_2O_4$- to $Ni(OH)_2$-like phases. This can be illustrated through the Fe_{Td}-to-Fe_{Oh} coordination number ratio (Fig. 5a), which equals 1 for nickel ferrites, but decreases as [Ni] increases. Furthermore, the Ni-Fe_{Oh} distance increases (Fig. S7a) with increasing Ni concentration, approaching the values found for the $Ni(OH)_2$ reference. The presence of $Ni(OH)_2$ is also confirmed by the absence of the third Ni-Fe/Ni path for high Ni concentrations (Fig. S7b). For intermediate concentrations ($[Ni]_s$ = 2.3 to 9.4 atom nm^{-2}), it is difficult to pinpoint the exact Ni speciation. An R value between 3.0 and 3.3 Å can also be attributed to polynuclear complexes.[80] In the case of R0.1, at low Ni concentration ($[Ni]_s$ = 0.4 atom nm^{-2}), only ~3.5 Fe/Ni atoms were found at 3.01, 3.54 and 5.15 Å (Table 2). Similar trends are observed in Fe_{Td}/Fe_{Oh} (Fig. S7a) and in the R value of the first Ni-Fe/Ni that increases from 3.01 to 3.08 Å, when Ni concentration increases. Compared to R0.5 the

438 Fe_{Td}/Fe_{Oh} ratio is smaller, suggesting a greater proportion of $Ni(OH)_2$ precipitate when Ni is in the
439 presence of non-stoichiometric magnetite.

440 **Table 2** Structural parameters deduced from the EXAFS analysis at the Ni *K*-edge for different Ni concentrations on R0.5 ($[Ni]_s$
441 = 0.5 and 20.4 atom nm^{-2}) and R0.1 ($[Ni]_s$ = 0.4 and 22.6 atom nm^{-2}), and for $Ni(OH)_2$ reference. CN: coordination number, R:
442 interatomic distance (Å), σ^2: Debye-Waller factor ($Å^2$). E_0 is the energy shift parameter (eV). Uncertainties in CN, R and σ^2 are
443 estimated to be ± 10%, 1% and 20%, respectively. For $[Ni]_s$ = 0.5 and 0.4 atom nm^{-2}, the three Ni-Fe/Ni paths were fixed after
444 preliminary adjustments. Constrained parameters are denoted by "*".

Sample		**Path**				**Parameters**		
		Ni-O	**Ni-Fe/Ni**	**Ni-Fe/Ni**	**Ni-Fe/Ni**	**E_0**	**Reduced-chi²**	**R-factor**
$Ni(OH)_2$	**CN**	5.5	5.8			-2.9	12.60	0.03
	R	2.04	3.09					
	σ^2	0.009	0.007					
$[Ni]_s$ = 0.5 atom nm^{-2} (R0.5)	**CN**	6.1	6.2*	6.2*	6.2*	-1.5	8.57	0.03
	R	2.05	2.98	3.52	5.14			
	σ^2	0.005	0.009	0.010	0.002			
$[Ni]_s$ = 20.4 atom nm^{-2} (R0.5)	**CN**	6.0	3.8	1.8		-2.8	11.18	0.03
	R	2.04	3.07	3.54				
	σ^2	0.006	0.007	0.009				
$[Ni]_s$ = 0.4 atom nm^{-2} (R0.1)	**CN**	5.9	3.5*	3.5*	3.5*	-2.3	10.50	0.06
	R	2.04	3.01	3.54	5.15			
	σ^2	0.005	0.008	0.010	0.004			
$[Ni]_s$ = 22.6 atom nm^{-2} (R0.1)	**CN**	6.0	4.2	1.0		-2.7	11.61	0.02
	R	2.04	3.08	3.58				
	σ^2	0.005	0.006	0.007				

445

The results indicate different Ni speciation depending on [Ni] and magnetite stoichiometry. Thus, at low Ni concentration, the Ni seems to be incorporated into the R0.5 (Fig. 6a), and to adsorb on the surface of R0.1 by forming an edge-sharing complex with three FeO_6 (Oh) and corner-sharing complex with three FeO_4 (Td) (Fig. 6b). On the other hand, at high Ni concentrations, its behavior is similar with R0.1 and R0.5 because it precipitates as $Ni(OH)_2$.

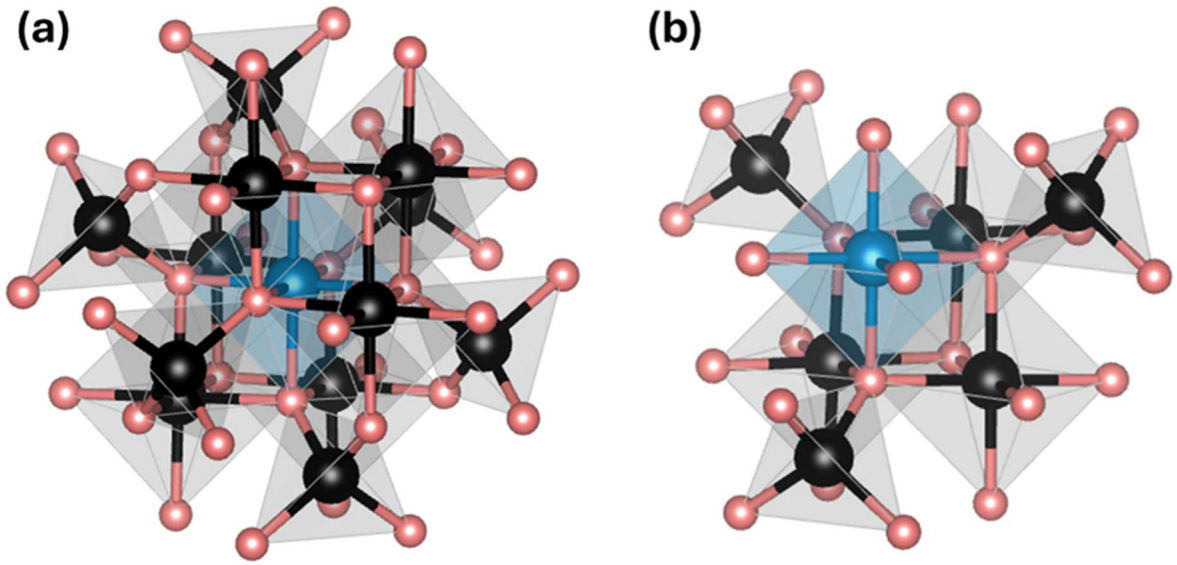

Fig. 6 Proposed structures for low [Ni]. (a) Ni incorporated in stoichiometric magnetite (R0.5) in a $NiFe_2O_4$-like structure, and (b) Ni adsorbed on the surface of non-stoichiometric magnetite (R0.1) by forming an edge-sharing complexes with three octahedral Fe (FeO_6) and corner-sharing complexes with three tetrahedral Fe (FeO_4). Blue balls: Ni. Black balls: Fe. Red balls: O.

4. Conclusion

The present study provides new insights into interactions between Ni and $Fe_{3-\delta}O_4$ nanoparticles, taking, emphasizing the influence of magnetite stoichiometry and pH on Ni speciation. Key mechanisms include Ni incorporation as $NiFe_2O_4$-like structure, surface complex formation, and precipitation of $Ni(OH)_2$-like phases. Compared to Co, Ni shows weaker interactions with oxidized magnetite (R0.1), likely due to its less flexible redox behavior and larger ionic radius. At trace levels, Ni incorporation is enhanced in stoichiometric magnetite (R0.5), where Fe(II) plays a critical role in facilitating dynamic metal uptake.

These findings underline the importance of magnetite stoichiometry in controlling Ni interactions, with implications for remediation applications and the synthesis of Ni-doped magnetite nanoparticles for environmental and technological purposes. Furthermore, this study highlights the role of redox-sensitive magnetite-maghemite solid solutions, commonly found in soils and sediments subjected to redox fluctuations, in influencing Ni behaviour, bioavailability and toxicity.

Finally, while Ni and Co share similarities as neighboring elements, their differing behaviors with magnetite highlight the complexity of surface speciation, which remains element-dependent. This underscores the challenges of developing predictive models for metal interactions with magnetite compared to other Fe-(hydr)oxides. Further research is needed to integrate the unique properties of magnetite into geochemical and surface speciation models to improve predictions of metal fate and ecotoxicity in both natural and anthropogenic environments.

Author contributions

Laura Fablet: writing-original draft, data curation, investigation, visualization. Mathieu Pédrot: writing – review & editing, data curation, investigation, resources, supervision, project administration, funding acquisition. Fadi Choueikani: writing – review & editing, data curation, investigation, resources, supervision, project administration, funding acquisition. Isabelle Kieffer: data curation, writing – review & editing. Olivier Proux: data curation, writing – review & editing. Anne-Catherine Pierson-Wickmann: data curation, investigation, writing – review & editing. Vyria Cagnart: data curation, investigation. Takumi Yomogida: data curation, investigation. Rémi Marsac: writing – review & editing, data curation, investigation, resources, supervision, project administration, funding acquisition.

Conflicts of interest

There are no conflicts to declare.

Data availability statement

The data supporting this article have been included as part of the Supplementary Information, in the IPGP Research Collection (https://doi.org/10.18715/IPGP.2024.m20b4bsd), or on the ESRF data portal (https://doi.org/10.15151/ESRF-ES-903899237).

Acknowledgments

This work was supported by the French Brittany Region (ARED project "NANOMAG"), SOLEIL synchrotron, the "COLOSSAL" project funded by ANR (project number ANR-23-CE01-0001) and the MADMAG project funded by the CNRS-INSU EC2CO program. Through the support of the GeOHeLiS analytical platform of Rennes University, this publication is also supported by the European Union through the European Regional Development Fund (FEDER), the French Ministry of Higher Education and Research, the French Region of Brittany and Rennes Metropole. The authors further acknowledge the SOLEIL and ESRF synchrotron for beamtime allocation at the DEIMOS beamline (proposal no. 20221130) and the FAME-UHD beamline (proposal no. 20220652, A16-1-816). The FAME-UHD project is financially supported by the French "grand emprunt" EquipEx (MAGNIFIX, ANR-21-ESRE-0011), the French "Programmes et équipements prioritaires de recherche" (DIADEM), the CEA-CNRS CRG consortium and the INSU CNRS institute. The authors are grateful to L. Dutruch and M. Pattier for assistance in ICP-MS and UV-vis analysis, as well as V. Dorcet and L. Rault for assistance in TEM experiments performed on

the THEMIS platform (ScanMAT, UMS 2011 University of Rennes-CNRS; CPER-FEDER 2007–2014).

References

1 Yahaya Ahmed Iyaka, Nickel in soils: A review of its distribution and impacts, *Sci. Res. Essays*, DOI:10.5897/SREX11.035.

2 T. V. M. Sreekanth, P. C. Nagajyothi, K. D. Lee and T. N. V. K. V. Prasad, Occurrence, physiological responses and toxicity of nickel in plants, *Int. J. Environ. Sci. Technol.*, 2013, **10**, 1129–1140.

3 B. Shahzad, M. Tanveer, A. Rehman, S. A. Cheema, S. Fahad, S. Rehman and A. Sharma, Nickel; whether toxic or essential for plants and environment - A review, *Plant Physiol. Biochem.*, 2018, **132**, 641–651.

4 P. H. Brown, R. M. Welch and E. E. Cary, Nickel: A Micronutrient Essential for Higher Plants 1, *Plant Physiol.*, 1987, **85**, 801–803.

5 S. B. Mulrooney and R. P. Hausinger, Nickel uptake and utilization by microorganisms, *FEMS Microbiol. Rev.*, 2003, **27**, 239–261.

6 C. Vischetti, E. Marini, C. Casucci and A. De Bernardi, Nickel in the Environment: Bioremediation Techniques for Soils with Low or Moderate Contamination in European Union, *Environments*, 2022, **9**, 133.

7 B. J. Alloway, *Heavy Metals in Soils*, Springer Science & Business Media, 1995.

8 D. E. Salt, N. Kato, U. Krämer, R. D. Smith and I. Raskin, in *Phytoremediation of Contaminated Soil and Water*, CRC Press, 2000.

9 C. Reimann, K. Fabian, M. Birke, P. Filzmoser, A. Demetriades, P. Négrel, K. Oorts, J. Matschullat, P. de Caritat, S. Albanese, M. Anderson, R. Baritz, M. J. Batista, A. Bel-lan, D. Cicchella, B. De Vivo, W. De Vos, E. Dinelli, M. Ďuriš, A. Dusza-Dobek, O. A. Eggen, M. Eklund, V. Ernsten, D. M. A. Flight, S. Forrester, U. Fügedi, A. Gilucis, M. Gosar, V. Gregorauskiene, W. De Groot, A. Gulan, J. Halamić, E. Haslinger, P. Hayoz, J. Hoogewerff, H. Hrvatovic, S. Husnjak, F. Jähne-Klingberg, L. Janik, G. Jordan, M. Kaminari, J. Kirby, V. Klos, P. Kwećko, L. Kuti, A. Ladenberger, A. Lima, J. Locutura, P. Lucivjansky, A. Mann, D. Mackovych, M. McLaughlin, B. I. Malyuk, R. Maquil, R. G. Meuli, G. Mol, P. O'Connor, R. T. Ottesen, A. Pasnieczna, V. Petersell, S. Pfleiderer, M. Poňavič, C. Prazeres, S. Radusinović, U. Rauch, I. Salpeteur, R. Scanlon, A. Schedl, A. Scheib, I. Schoeters, P. Šefčik, E. Sellersjö, I. Slaninka, J. M. Soriano-Disla, A. Šorša, R. Svrkota, T. Stafilov, T. Tarvainen, V. Tendavilov, P. Valera, V. Verougstraete, D. Vidojević, A. Zissimos, Z. Zomeni and M. Sadeghi, GEMAS: Establishing geochemical background and threshold for 53 chemical elements in European agricultural soil, *Appl. Geochem.*, 2018, **88**, 302–318.

10 C. Tsadilas, J. Rinklebe and M. Selim, *Nickel in Soils and Plants*, CRC Press, 2018.

11 M. Cempel and G. Nikel, Nickel: A Review of Its Sources and Environmental Toxicology, *Pol. J. Environ. Stud.*

12 S. Bhalerao, A. Sharma and A. Poojari, Toxicity of Nickel in Plants, *Int. J. Appl. Biosci.*, 2015, **3**, 345–355.

13 T. A. Blewett and E. M. Leonard, Mechanisms of nickel toxicity to fish and invertebrates in marine and estuarine waters, *Environ. Pollut.*, 2017, **223**, 311–322.

14 K. Nithya, A. Sathish, P. Senthil Kumar and T. Ramachandran, Fast kinetics and high adsorption capacity of green extract capped superparamagnetic iron oxide nanoparticles for the adsorption of Ni(II) ions, *J. Ind. Eng. Chem.*, 2018, **59**, 230–241.

15 V. Sharma, H. Singh, S. Guleria, N. Bhardwaj, S. Puri, S. K. Arya and M. Khatri, Application of superparamagnetic iron oxide nanoparticles (SPIONs) for heavy metal adsorption: A 10-year meta-analysis, *Environ. Nanotechnol. Monit. Manag.*, 2022, **18**, 100716.

16 A. J. Frierdich and J. G. Catalano, Controls on Fe(II)-Activated Trace Element Release from Goethite and Hematite, *Environ. Sci. Technol.*, 2012, **46**, 1519–1526.

17 M. Wang and Y. Yin, Magnetically Responsive Nanostructures with Tunable Optical Properties, *J. Am. Chem. Soc.*, 2016, **138**, 6315–6323.

18 M. Hua, S. Zhang, B. Pan, W. Zhang, L. Lv and Q. Zhang, Heavy metal removal from water/wastewater by nanosized metal oxides: A review, *J. Hazard. Mater.*, 2012, **211–212**, 317–331.
19 P. J. Borm, D. Robbins, S. Haubold, T. Kuhlbusch, H. Fissan, K. Donaldson, R. Schins, V. Stone, W. Kreyling, J. Lademann, J. Krutmann, D. Warheit and E. Oberdorster, The potential risks of nanomaterials: a review carried out for ECETOC, *Part. Fibre Toxicol.*, 2006, **3**, 11.
20 R. M. Cornell and U. Schwertmann, *The Iron Oxides: Structure, Properties, Reactions, Occurences and Uses*, Wiley-VCH: Berlin, 1st edn., 2003.
21 G. S. Parkinson, Iron oxide surfaces, *Surf. Sci. Rep.*, 2016, **71**, 272–365.
22 D. Faivre and T. U. Godec, From Bacteria to Mollusks: The Principles Underlying the Biomineralization of Iron Oxide Materials, *Angew. Chem. Int. Ed.*, 2015, **54**, 4728–4747.
23 M. Ovais, A. T. Khalil, M. Ayaz, I. Ahmad, S. K. Nethi and S. Mukherjee, Biosynthesis of Metal Nanoparticles via Microbial Enzymes: A Mechanistic Approach, *Int. J. Mol. Sci.*, 2018, **19**, 4100.
24 S. I. Siddiqui and S. A. Chaudhry, Iron oxide and its modified forms as an adsorbent for arsenic removal: A comprehensive recent advancement, *Process Saf. and Environ. Prot.*, 2017, **111**, 592–626.
25 D. Fortin and S. Langley, Formation and occurrence of biogenic iron-rich minerals, *Earth-Sci. Rev.*, 2005, **72**, 1–19.
26 W. Kündig and R. Steven Hargrove, Electron hopping in magnetite, *Solid State Commun.*, 1969, **7**, 223–227.
27 P. Majewski and B. Thierry, Functionalized Magnetite Nanoparticles—Synthesis, Properties, and Bio-Applications, *Crit. Rev. Solid State Mater*, 2007, **32**, 203–215.
28 Y. Mamindy-Pajany, S. Sayen, J. F. W. Mosselmans and E. Guillon, Copper, Nickel and Zinc Speciation in a Biosolid-Amended Soil: pH Adsorption Edge, μ-XRF and μ-XANES Investigations, *Environ. Sci. Technol.*, 2014, **48**, 7237–7244.
29 L. Zhu, X. Zhang, J. Zhang, T. Liu and Y. Qiu, Saltwater intrusion weakens Fe-(oxyhydr)oxide-mediated (im)mobilization of Ni and Zn in redox-fluctuating soil–groundwater system, *Water Res.*, 2022, **221**, 118799.
30 N. Boujelben, J. Bouzid and Z. Elouear, Adsorption of nickel and copper onto natural iron oxide-coated sand from aqueous solutions: Study in single and binary systems, *J. Hazard. Mater.*, 2009, **163**, 376–382.
31 Y. Xu, L. Axe, T. Boonfueng, T. A. Tyson, P. Trivedi and K. Pandya, Ni(II) complexation to amorphous hydrous ferric oxide: An X-ray absorption spectroscopy study, *J. Colloid Interface Sci.*, 2007, **314**, 10–17.
32 Y. Arai, Spectroscopic Evidence for Ni(II) Surface Speciation at the Iron Oxyhydroxides−Water Interface, *Environ. Sci. Technol.*, 2008, **42**, 1151–1156.
33 N. Azimi, P. Azimi, M. Samimi and T. Mansouri Jalilian, Ultrasonic-assisted adsorption of Ni(II) ions from aqueous solution onto Fe_3O_4 nanoparticles, *Adv. Nanochem.*, 2019, **1**, 66–72.
34 Y. C. Sharma and V. Srivastava, Comparative Studies of Removal of Cr(VI) and Ni(II) from Aqueous Solutions by Magnetic Nanoparticles, *J. Chem. Eng. Data*, 2011, **56**, 819–825.
35 M. R. Lasheen, I. Y. El-Sherif, D. Y. Sabry, S. T. El-Wakeel and M. F. El-Shahat, Adsorption of heavy metals from aqueous solution by magnetite nanoparticles and magnetite-kaolinite nanocomposite: equilibrium, isotherm and kinetic study, *Desalin. Water Treat.*, 2016, **57**, 17421–17429.
36 N. N. Nassar, Kinetics, equilibrium and thermodynamic studies on the adsorptive removal of nickel, cadmium and cobalt from wastewater by superparamagnetic iron oxide nanoadsorbents, *Can. J. Chem. Eng.*, 2012, **90**, 1231–1238.

37 Y. F. Shen, J. Tang, Z. H. Nie, Y. D. Wang, Y. Ren and L. Zuo, Preparation and application of magnetic Fe_3O_4 nanoparticles for wastewater purification, *Sep. Purif. Technol.*, 2009, **68**, 312–319.
38 X. S. Wang, J. J. Ren, H. J. Lu, L. Zhu, F. Liu, Q. Q. Zhang and J. Xie, Removal of Ni(II) from Aqueous Solutions by Nanoscale Magnetite, *CLEAN – Soil, Air, Water*, 2010, **38**, 1131–1136.
39 C. A. Gorski, R. M. Handler, B. L. Beard, T. Pasakarnis, C. M. Johnson and M. M. Scherer, Fe Atom Exchange between Aqueous Fe^{2+} and Magnetite, *Environ. Sci. Technol.*, 2012, **46**, 12399–12407.
40 P. Jungcharoen, M. Pédrot, F. Choueikani, M. Pasturel, K. Hanna, F. Heberling, M. Tesfa and R. Marsac, Probing the effects of redox conditions and dissolved Fe^{2+} on nanomagnetite stoichiometry by wet chemistry, XRD, XAS and XMCD, *Environ. Sci.: Nano*, 2021, **8**, 2098–2107.
41 P. Jungcharoen, M. Pédrot, F. Heberling, K. Hanna, F. Choueikani, C. Catrouillet, A. Dia and R. Marsac, Prediction of nanomagnetite stoichiometry (Fe(II)/Fe(III)) under contrasting pH and redox conditions, *Environ. Sci.: Nano*, 2022, **9**, 2363–2371.
42 L. Fablet, F. Choueikani, M. Pédrot, M. Kerdiles, M. Pasturel and R. Marsac, Investigation of magnetite–Co interactions: from environmentally relevant trace Co levels to core–shell Fe_3O_4@$Co(OH)_2$ nanoparticles with magnetic applications, *Environ. Sci.: Nano*, 2023, **10**, 3051–3061.
43 L. Fablet, F. Choueikani, M. Pédrot and R. Marsac, What are the effects of environmental factors on Co speciation at the magnetite surface?, *Environ. Sci.: Nano*, 2024, **11**, 2036–2048.
44 R. Massart, Preparation of aqueous magnetic liquids in alkaline and acidic media, *IEEE Trans. Magn.*, 1981, **17**, 1247–1248.
45 W. B. Fortune and M. G. Mellon, Determination of Iron with o-Phenanthroline: A Spectrophotometric Study, *Ind. Eng. Chem. Anal. Ed.*, 1938, **10**, 60–64.
46 D. Yeghicheyan, D. Aubert, M. Bouhnik-Le Coz, J. Chmeleff, S. Delpoux, I. Djouraev, G. Granier, F. Lacan, J.-L. Piro, T. Rousseau, C. Cloquet, A. Marquet, C. Menniti, C. Pradoux, R. Freydier, E. Vieira da Silva-Filho and K. Suchorski, A New Interlaboratory Characterisation of Silicon, Rare Earth Elements and Twenty-Two Other Trace Element Concentrations in the Natural River Water Certified Reference Material SLRS-6 (NRC-CNRC), *Geostand. Geoanalytical Res.*, 2019, **43**, 475–496.
47 P. Ohresser, E. Otero, F. Choueikani, K. Chen, S. Stanescu, F. Deschamps, T. Moreno, F. Polack, B. Lagarde, J.-P. Daguerre, F. Marteau, F. Scheurer, L. Joly, J.-P. Kappler, B. Muller, O. Bunau and Ph. Sainctavit, DEIMOS: A beamline dedicated to dichroism measurements in the 350–2500 eV energy range, *Rev. Sci. Instrum.*, 2014, **85**, 013106.
48 S. Brice-Profeta, M.-A. Arrio, E. Tronc, N. Menguy, I. Letard, C. Cartier dit Moulin, M. Noguès, C. Chanéac, J.-P. Jolivet and Ph. Sainctavit, Magnetic order in γ-Fe_2O_3 nanoparticles: a XMCD study, *J. Magn. Magn. Mater.*, 2005, **288**, 354–365.
49 L. Joly, E. Otero, F. Choueikani, F. Marteau, L. Chapuis and P. Ohresser, Fast continuous energy scan with dynamic coupling of the monochromator and undulator at the DEIMOS beamline, *J. Synchrotron Rad.*, 2014, **21**, 502–506.
50 D. L. Parkhurst and C. A. J. Appelo, User's guide to PHREEQC (Version 2): A computer program for speciation, batch-reaction, one-dimensional transport, and inverse geochemical calculations, *Water Resour. Invest. Rep.*, 1999, 99–4259.
51 D. A. Dzombak and F. M. M. Morel, *Surface Complexation Modeling: Hydrous Ferric Oxide*, John Wiley & Sons, New York, 1991.
52 T. Missana, C. Maffiotte and M. García-Gutiérrez, Surface reactions kinetics between nanocrystalline magnetite and uranyl, *J. Colloid Interface Sci.*, 2003, **261**, 154–160.

53 J.-W. Moon, Y. Roh, R. J. Lauf, H. Vali, L. W. Yeary and T. J. Phelps, Microbial preparation of metal-substituted magnetite nanoparticles, *J. Microbiol. Methods*, 2007, **70**, 150–158.
54 R. Bliem, J. Pavelec, O. Gamba, E. McDermott, Z. Wang, S. Gerhold, M. Wagner, J. Osiecki, K. Schulte, M. Schmid, P. Blaha, U. Diebold and G. S. Parkinson, Adsorption and incorporation of transition metals at the magnetite Fe_3O_4 (001) surface, *Phys. Rev. B*, 2015, **92**, 075440.
55 T. Hiemstra and W. H. Van Riemsdijk, A Surface Structural Approach to Ion Adsorption: The Charge Distribution (CD) Model, *J. Colloid Interface Sci.*, 1996, **179**, 488–508.
56 W. Cheng, R. Marsac and K. Hanna, Influence of Magnetite Stoichiometry on the Binding of Emerging Organic Contaminants, *Environ. Sci. Technol.*, 2018, **52**, 467–473.
57 K. J. Farley, D. A. Dzombak and F. M. M. Morel, A surface precipitation model for the sorption of cations on metal oxides, *J. Colloid Interface Sci.*, 1985, **106**, 226–242.
58 J. Lutzenkirchen and Ph. Behra, On the surface precipitation model for cation sorption at the (hydr)oxide water interface, *Aquat. Geochem.*, 1996, **1**, 375–397.
59 T. M. Petrova, L. Fachikov and J. Hristov, The magnetite as adsorbent for some hazardous species from aqueous solutions: a review, *Int. Rev. Chem. Eng.*, 2011, **3**, 19.
60 G. Sposito, The “physics” of soil water physics, *Water Resources Research*, 1986, **22**, 83S-88S.
61 W. Stumm and J. J. Morgan, *Aquatic Chemistry: Chemical Equilibria and Rates in Natural Waters*, John Wiley & Sons, 2013.
62 P. R. Tremaine and J. C. Leblanc, The solubility of nickel oxide and hydrolysis of Ni^{2+} in water to 573 K, *J. Chem. Thermodyn.*, 1980, **12**, 521–538.
63 N. V. Plyasunova, Y. Zhang and M. Muhammed, Critical evaluation of thermodynamics of complex formation of metal ions in aqueous solutions. V. hydrolysis and hydroxo-complexes of Co^{2+} at 298.15 K, *Hydrometallurgy*.
64 R. D. Shannon, Revised effective ionic radii and systematic studies of interatomic distances in halides and chalcogenides, *Acta Cryst. A*, 1976, **32**, 751–767.
65 K. SARTORI, Thesis, Université de Strasbourg, 2019.
66 M. M. Natile and A. Glisenti, New NiO/Co_3O_4 and Fe_2O_3/Co_3O_4 Nanocomposite Catalysts: Synthesis and Characterization, *Chem. Mater.*, 2003, **15**, 2502–2510.
67 A. Tougerti, I. Llorens, F. D’Acapito, E. Fonda, J.-L. Hazemann, Y. Joly, D. Thiaudière, M. Che and X. Carrier, Surface Science Approach to the Solid–Liquid Interface: Surface-Dependent Precipitation of $Ni(OH)_2$ on α-Al_2O_3 Surfaces, *Ang. Chem. Int. Ed.*, 2012, **51**, 7697–7701.
68 R. Qiao, L. A. Wray, J.-H. Kim, N. P. W. Pieczonka, S. J. Harris and W. Yang, Direct Experimental Probe of the Ni(II)/Ni(III)/Ni(IV) Redox Evolution in $LiNi_{0.5}Mn_{1.5}O_4$ Electrodes, *J. Phys. Chem. C*, 2015, **119**, 27228–27233.
69 D. Asakura, E. Hosono, Y. Nanba, H. Zhou, J. Okabayashi, C. Ban, P.-A. Glans, J. Guo, T. Mizokawa, G. Chen, A. J. Achkar, D. G. Hawthron, T. Z. Regier and H. Wadati, Material/element-dependent fluorescence-yield modes on soft X-ray absorption spectroscopy of cathode materials for Li-ion batteries, *AIP Adv.*, 2016, **6**, 035105.
70 J. Jeong, K. J. Park, E.-J. Cho, H.-J. Noh, S. B. Kim and H.-D. Kim, Electronic structure change of $NiS_{2-x}Se_x$ in the metal-insulator transition probed by X-ray absorption spectroscopy, *J. Korean Phys. Soc.*, 2018, **72**, 111–115.
71 M. Landers, M. Gräfe, R. J. Gilkes, M. Saunders and M. A. Wells, Nickel distribution and speciation in rapidly dehydroxylated goethite in oxide-type lateritic nickel ores: XAS and TEM spectroscopic (EELS and EFTEM) investigation, *Aust. J. Earth Sci.*, 2011, **58**, 745–765.
72 D. Friebel, M. W. Louie, M. Bajdich, K. E. Sanwald, Y. Cai, A. M. Wise, M.-J. Cheng, D. Sokaras, T.-C. Weng, R. Alonso-Mori, R. C. Davis, J. R. Bargar, J. K. Nørskov, A. Nilsson

and A. T. Bell, Identification of Highly Active Fe Sites in (Ni,Fe)OOH for Electrocatalytic Water Splitting, *J. Am. Chem. Soc.*, 2015, **137**, 1305–1313.
73 G. Wei, X. Liang, Z. He, Y. Liao, Z. Xie, P. Liu, S. Ji, H. He, D. Li and J. Zhang, Heterogeneous activation of Oxone by substituted magnetites $Fe_{3-x}M_xO_4$ (Cr, Mn, Co, Ni) for degradation of Acid Orange II at neutral pH, *J. Mol. Catal. A: Chem.*, 2015, **398**, 86–94.
74 D. K. Bediako, B. Lassalle-Kaiser, Y. Surendranath, J. Yano, V. K. Yachandra and D. G. Nocera, Structure–Activity Correlations in a Nickel–Borate Oxygen Evolution Catalyst, *J. Am. Chem. Soc.*, 2012, **134**, 6801–6809.
75 C. M. B. Henderson, J. M. Charnock and D. A. Plant, Cation occupancies in Mg, Co, Ni, Zn, Al ferrite spinels: a multi-element EXAFS study, *J. Phys.: Condens. Matter*, 2007, **19**, 076214.
76 K. I. Pandya, W. E. O'Grady, D. A. Corrigan, J. McBreen and R. W. Hoffman, Extended x-ray absorption fine structure investigations of nickel hydroxides, *J. Phys. Chem.*, 1990, **94**, 21–26.
77 X. Tan, J. Hu, G. Montavon and X. Wang, Sorption Speciation of Nickel(II) onto Ca-Montmorillonite: Batch, EXAFS Techniques and Modeling, *Dalton Trans.*, 2011, **40**, 10953–10960.
78 X. Liang, Z. He, W. Tan, P. Liu, J. Zhu, J. Zhang and H. He, The oxidation state and microstructural environment of transition metals (V, Co, and Ni) in magnetite: an XAFS study, *Phys. Chem. Minerals*, 2015, **42**, 373–383.
79 M. H. Nilsen, C. Nordhei, A. L. Ramstad, D. G. Nicholson, M. Poliakoff and A. Cabañas, XAS (XANES and EXAFS) Investigations of Nanoparticulate Ferrites Synthesized Continuously in Near Critical and Supercritical Water, *J. Phys. Chem. C*, 2007, **111**, 6252–6262.
80 O. Saensuk, S. Phokha, A. Bootchanont, S. Maensiri and E. Swatsitang, Fabrication and magnetic properties of $NiFe_2O_4$ nanofibers obtained by electrospinning, *Ceram. Int.*, 2015, **41**, 8133–8141.
81 D. Carta, D. Loche, G. Mountjoy, G. Navarra and A. Corrias, $NiFe_2O_4$ Nanoparticles Dispersed in an Aerogel Silica Matrix: An X-ray Absorption Study, *J. Phys. Chem. C*, 2008, **112**, 15623–15630.